Cronfa - Swansea University Open Access Repository

_____

This is an author produced version of a paper published in:
Angewandte Chemie International Edition

_____

Cronfa URL for this paper:
http://cronfa.swan.ac.uk/Record/cronfa34514

_____

Paper:

Sottmann, J., Dimichel, M., Fjellvåg, H., Malavasi, L., Margadonna, S., Vajeeston, P., Vaughan, G. & Wragg, D. (2017). Chemical structure of specific sodium ion battery components with operando pair distribution function and X-ray diffraction computed tomography. _Angewandte Chemie International Edition_
http://dx.doi.org/10.1002/anie.201704271

_____

http://www.swansea.ac.uk/iss/researchsupport/cronfa-support/

Chemical structure of specific sodium ion battery components with operando pair distribution function and X-ray diffraction computed tomography

Jonas Sottmann[†], Marco Di Michiel[‡], Helmer Fjellvåg[†], Lorenzo Malavasi[#], Serena Margadonna[§*], Ponniah Vajeeston[†], Gavin Vaughan[‡], David S. Wragg[†*]

[†] Department of Chemistry, University of Oslo, Blindern, P.O. Box 1033, 0315 Oslo, Norway.

[‡] ESRF - The European Synchrotron, CS40220, 38043 Grenoble, France.

[§] College of Engineering, Swansea University, Swansea SA1 8EN, UK.

[#] Department of Chemistry, University of Pavia and INSTM, Viale Taramelli 16, 27100 Pavia – ITALY.

*corresponding authors

Abstract: To improve lithium and sodium ion battery technology it is imperative to understand how the properties of the different components are controlled by their chemical structures. Operando structural studies give us some of the most useful information for understanding how batteries work, but it remains difficult to separate out the contributions of the various components of a battery stack (e.g. electrodes, current collectors, electrolyte and binders) and examine specific materials. We have used operando X-ray diffraction computed tomography (XRD-CT) to study specific components of an essentially unmodified, working cell and extract detailed, space resolved structural information on both crystalline and amorphous phases present during cycling by Rietveld and pair distribution function (PDF) methods. We illustrate this method with the first detailed structural examination of the cycling of sodium in a phosphorus anode, revealing surprisingly different mechanisms for sodiation and desodiation in this promising, high capacity anode system.

One of the biggest problems in studying battery structures in general, and in particular when using total X-ray scattering methods, is the contribution to the data from parts of the battery other than those in which we are interested[1]. This is less significant for conventional X-ray diffraction studies of crystalline materials where it is usually possible to mask the background features and concentrate on the Bragg peaks from the component of interest[2]. Unfortunately, many of the most interesting battery materials are amorphous at some stages of cycling. Studying amorphous materials with X-ray scattering requires us to use the total scattering of the sample to calculate the PDF. To do this the non-sample contributions must be removed.[3] Allan et al[4] and Chapman et al[5] have addressed this by using background subtraction methods and adapting their batteries significantly for total scattering experiments. Here we propose an alternative and much more informative method based on the PDF-CT approach first reported by Jacques et al[6]. Although operando tomographic imaging has recently revealed significant information on the macrostructure of batteries[7] and been combined with scanning XRD[8], the tomographic technique has not been applied using atomic structural data. Jensen et al studied commercial

lithium ion and nickel metal hydride batteries with XRD-CT methods, mapping the distribution of $LiCoO_2$ from the intensity of a single peak and obtaining information on its orientation from the 2D diffraction patterns[9]. By reconstructing the entire battery system with XRD-CT and carrying out Rietveld and PDF analysis of the data as a function of charge state we have, firstly, obtained data focussing specifically on the phosphorus anode of a basically unmodified (i.e. not significantly different from a normal coin cell; this may be compared to the highly adapted electrode particles studied with absorption CT by Ebner et al.[7b]), working sodium ion battery (SIB) and secondly, removed all contributions from the other components of the cell and sample container, giving the best quality data on the anode for Rietveld and PDF analysis. As we have shown elsewhere[10], the use of full structural methods allows data to be extracted from tomograms which would have been considered useless if analysed with conventional phase contrast and absorption tomography techniques.

Phosphorus is one of the most promising alloying anodes for SIBs due to its high capacity (theoretical capacity 2596 mAh g^{-1}, reversible capacity of up to 1890 mAh g^{-1} as a composite with carbon and considerable cycling stability[11]). Its structure has not previously been studied under working conditions and is amorphous except when fully sodiated to form crystalline Na_3P[12]. Combined *operando* XRD/PDF-CT reveals with full clarity the different mechanisms of sodiation and desodiation of phosphorus (despite its low X-ray scattering factor and location inside an electrochemical cell), in good agreement with cycling data and density functional theory (DFT) calculations. The technique described here was also combined with *operando* X- ray absorption tomographic imaging to provide additional information on the battery's macrostructure (e.g. volume changes, dendrite formation). This allows us to identify potential problems such as movement and expansion of the battery components, particularly relevant for alloying anodes like phosphorus which can undergo volume changes of as much as 400 % during cycling (see ESI movie).

Initial analysis of the reconstructed XRD-CT data for the anode region using "surface" Rietveld methods (with the crystalline Na_3P structure) showed limited structural variations within the individual tomographic slices (Figure 1), but confirmed the stability of the methods and the location of the anode material at this stage. Slices 4 and 5 of the tomogram contain significant amounts of glass fibre separating material, with slice 5 containing virtually no anode material despite the volume expansion. The resolution of the tomograms in XRD-CT is limited by the size of the beam (see experimental section) and was also optimised to give enough tomograms during battery cycling to see the structure at different points in the charge/discharge curve. Improvements in both beam

line optics and detector technology (in place at ID15 since January 2017) will improve the space and time resolution of the method, and may allow extraction of structural data from individual particles in future. Variations in the parameters between the layers are probably due principally to the changes in charge state during the 7 minute slice acquisition time (see charge states in Figure 3). The central section of slice 4, however, does seem to have a well determined Na3P c-axis parameter which is similar to that of slice 1 (close to the current collector). The reconstructed diffractograms from the centre of slices 2, 3 and 4 (ESI, Figure S17) are of similar quality. This may indicate that the reaction is at a different stage close to the electrolyte and current collector, than in the central slices. Note, however that sodiation is complete at slice 4, with the final capacity of 1471 mAhg^{-1} reached, while in slices 1, 2 and 3 sodiation is still in progress. It is therefore possible that the structure relaxes when the final, open circuit voltage is reached. Further analysis focussed on the central voxels of the slices. Reconstructed diffractograms of the voxel at position (15,15) in slice 3 for desodiation and second sodiation are shown in Figure 2. The Bragg peaks from the Na3P phase are clearly visible when the anode is fully sodiated and a broad feature in the diffraction patterns at $2\theta \approx 4\,°$ appears during sodiation but not during desodiation. The broad peak at ~2.5 ° is due to phosphorus nanoparticles.

Rietveld analysis of voxel (15,15) in tomographic slices 2 and 3 showed the appearance of the crystalline Na3P phase during sodiation and its disappearance during desodiation. Trends in the crystallite size, unit cell axes and occupancy of the Na atom sites of the layered Na3P structure are shown in Figure 3 along with the voltage profiles. A clear decline in crystallite size is observed during desodiation with a corresponding growth in the crystallite size during sodiation when the phase reappears. The two Na sites are seen to depopulate during desodiation and gradually repopulate as the Na3P phase reappears during sodiation. This suggests high mobility of Na in the phase, in agreement with the findings of Qian et al[11a]. High Na mobility was also observed in Na3Sb[4]. In addition, the occupancies of the Na sites never reach 100%, suggesting that stoichiometric Na3P is not formed. The lattice parameter data show small variations in the a-axis while the c-axis extends significantly during the first desodiation and contracts slightly during the second sodiation.

The fitted PDFs (G(r)) are shown in the ESI (Figure S3-S15), with the fit agreement factors (Table S1). Despite the high noise levels in the G(r)s during the amorphous stages of cycling, our models explain the key features of the PDFs. From the extent of the peaks in the PDF we extracted crystallite/cluster sizes at each charge state. The simplest possible cluster models were used in fitting to avoid fitting noise at high G(r) in the amorphous materials. Scale factors for the fitted

phases are plotted in Figure 4 with the voltage curves above. The crystallite size from the Rietveld refinement is plotted on the same axes for comparison. The G(r) when fully desodiated has only one peak at approx.

2.25 Å (the approximate length of a P-P bond) indicating a cluster of a few phosphorus atoms with no order beyond the first shell of P-P bonds. We fitted this using a model cluster of 4 P atoms (Figure 5).

The PDF analysis shows clearly that NaP (with a cluster size of less than 10 Å) is formed during sodiation but not during desodiation, while Na_3P is present for longer during desodiation. Compared to the Rietveld analysis of Na_3P we observe the phase later during desodiation and earlier during sodiation in the PDF data, suggesting that amorphous Na_3P exists before the crystalline form.

DFT calculations were used to construct a convex energy hull diagram for the Na/P system (Figure 6) which is in agreement with that reported by Mayo et al.[13] The hull shows the most thermodynamically favourable route between P and Na_3P. In agreement with our PDF results, the lowest energy route to Na_3P passes through the rather stable NaP helical P-chain structure (Figure 1b). This acts as an intermediate in a two phase type mechanism, easing the transition to layered Na_3P. We have so far found no evidence for the presence of any of the other stable Na/P phases lying on or close to the energy hull at any stage of cycling, though this cannot be entirely ruled out. It is possible that they may be observed with better time/space resolution and that the tiny clusters may exhibit varying

stoichiometry. These phases would further ease the transition from very small P clusters to the layered structure of Na_3P (see ESI). The NMR work of Xu et al also shows NaP as an intermediate structure[12b].

The energy hull does not help us to understand why the thermodynamic route is not followed on desodiation. We therefore carried out further calculations on the deintercalation of Na from Na_3P, maintaining the layered structure as observed in the *operando* tomographic experiment. We found that several stable phases exist, suggesting that a smooth transition from Na_3P through $Na_{3-x}P$ to P should be favoured by kinetics over the nucleation of NaP. i.e. in the case of high Na mobility as is the case here, NaP should not form. $Na_{2.6}P$ and $Na_{2.36}P$ are the possible stable Na deficient structures in the Na_3P matrix and are included as points in Figure 6 (the red dotted line indicates the kinetically favoured path from Na_3P to P). Furthermore, we calculated that Na_2P, which might serve as an intermediate on the path to NaP during desodiation, is highly unstable (this phase is also shown, well above the convex hull, in Figure 6). We believe that the small plateau observed at

~0.7 V during desodiation for phosphorene/graphene anodes[14] is a sign that the thermodynamic mechanism (Na3P-NaP-P) co-exists with the kinetic deintercalation mechanism to some degree at lower rates of desodiation. A similar kinetic mechanism was observed during desodiation of the Na/Sb system[4]. These mechanisms are supported by the lattice parameter values presented in Figure 3c. The large extension and small contraction of the c-axis during desodiation and second sodiation respectively indicate that the structure is retained for longer during desodiation, and that increasing levels of Na probably serve to hold the layered structure together.

The reasons for the different mechanisms of sodiation and desodiation of the group 15 elements are still unclear, though size effects may be significant. P (0.44 Å) and Sb (0.90 Å) have sodiation routes different from those of their desodiation, which include significant amorphous components. The somewhat larger Bi (1.03 Å[15]) follows the same route on sodiation and desodiation and retains crystallinity at all stages, with the crystal structure of Na3Bi depending on the crystallite size[16]. Also, the size of Bi is similar to that of Na^+ (1.02 Å effective ionic radius), while P and Sb are smaller. No experimental data on the Na/As system is available, although gallium arsenide has recently been studied as an anode for LIBs[17]. The rate of deintercalation of Na from crystalline Na3P is probably too rapid for the formation of intermediates except at very low rates of desodiation[11a, 14]. Na3Sb is similar, with the deintercalation leading to other clearly identifiable amorphous intermediates, but not NaSb[4]. The ^{23}Na NMR results reported by Allan and co-workers show high Na mobility (which they relate to the excellent high rate performance

of Sb anodes) in crystalline Na3Sb, which supports the idea that fast Na deintercalation is connected to the differences between sodiation and desodiation routes in P and Sb anodes[4]. The thermodynamic sodiation route from P nanoclusters to NaP chains to layered Na3P, involves the breaking and forming of many bonds and should be significantly slower than deintercalation.   A similar   scheme   with   kinetic   and thermodynamic routes for charge and discharge respectively is described for the Na/Co3O4 system[18].

Using XRD-CT methods allows us to study specific components of a working battery, obtaining high quality data with no additional signals beyond those from the component of interest, even for a weakly scattering material. This allows us to combine Rietveld analysis of the crystalline phases with PDF analysis of the amorphous material even in a moving or expanding electrode, as illustrated here by the example of an essentially unmodified, working phosphorus SIB anode. Our XRD-CT structural data combined with DFT calculations and cycling data show the different

structural mechanisms of sodiation and desodiation in the phosphorus anode. We believe this technique can offer very significant benefits for future structural studies of crystalline and amorphous battery materials.

Experimental

Amorphous phosphorus was prepared by milling red phosphorus (99.99 %, Sigma Aldrich) in a Fritsch Planetary Micro Mill Pulverisette 7 at 720 rpm with a ball-to-powder ratio of 20:1 for 24 h. A composite of amorphous phosphorus with CNTs (purified and multi-walled, n-tec) was formed by milling them in a mass ratio of 7:3 in a Fritsch Mini-Mill Pulverisette 23 at 50 Hz with a ball-to-powder ratio of 10:1 for 20 min. The working electrode was prepared by spreading slurry composed of 70 wt % of the composite, 10 wt % of conductive carbon black (Super P, Timcal) and 20 wt % poly(acrylicacid) (PAA, Sigma Aldrich) as binder dissolved in ethanol on the Al pistons used in the *operando* sample container. Drying of the electrodes was carried out at 60 °C overnight. The electrodes were thereafter handled under inert atmosphere. The working electrode was separated from the Na metal disk as counter electrode by electrolyte soaked glass fibres (GF/C, Whatman). As electrolyte a 1 M solution of $NaPF_6$ in ethylene carbonate/diethyl carbonate (EC/DEC, 1:1 in wt) solution with the addition of 5 wt % FEC was prepared. All electrolyte constituents were purchased from Sigma Aldrich. The battery was galvanostatically cycled in a voltage range of 0.01 V to 2 V vs Na/Na^+ using a Biologic SP150 with low current option. The specific capacity values are expressed on the basis of the mass of phosphorus.

Half cells were assembled in a specially constructed X-ray transparent electrochemical container for *operando* XRD/PDF-CT and absorption tomography measurements (see ESI). The sample container consists of a sealed Teflon cylinder containing two Al pistons on which working and Na metal counter electrode are directly deposited. The electrodes are separated by glass fibres soaked with electrolyte. The sample container is aligned such that the working electrode layer (about 30 μm thick and containing about 0.1 mg of amorphous phosphorous) oriented in plane with the X-ray beam and can be rotated by up to 360° around its vertical axis during the measurement. The thickness of the anode layer is slightly greater than normal, but otherwise this construction is very similar to what would be used in a coin cell for electrochemical testing,

Data were collected on beamline ID15A of the European Synchrotron (ESRF). The XRD/PDF-CT data were collected at an energy of 69.8 keV (λ = 0.1779 Å) with a beam size of 200×16 $μm^2$ (horizontal x vertical). Absorption tomography data were collected using a CMOS camera at an energy of 46.3 keV, field of view 1.3×1.3mm^2 and pixel size of 1.2×1.2μm^2). XRD/PDF-CT tomograms were collected with 5 vertical slices spaced by 8 μm followed by an absorption tomography measurement. The raw 2D diffraction images were azimuthally integrated to give 1D powder diffraction patterns which were used in the tomographic reconstruction. The strategy used for collection and reconstruction of the diffraction tomographic slices is described elsewhere[6, 19]. The data collection took about 7 min per slice for XRD/PDF-CT, while each absorption tomography measurement took about 15 min. The sequence of measurements was repeated

several times during the first desodiation and second sodiation of the Na/P half- cell, which lasted about 4 h.

Corrections were applied for artefacts in the filtered back projection tomogram caused by the Teflon walls of the sample container. A three dimensional map of the battery absorption coefficient was measured by a conventional absorption micro-tomography scan. An XRD-CT scan of the empty sample container was then measured. The absorption caused by the sample on the Teflon signal of the empty sample container was calculated using the 3-D absorption map. The calculation was done using a ray tracing program which computes the absorption correction for the diffracted signal generated by each voxel as a function of the sample orientation, 2-theta angle and azimuthal angle. The absorption corrected Teflon signal was removed from the battery diffraction signal for each voxel. The final reconstructed slices had a 30 x 30 voxel grid. The corrected diffractograms were processed using PDFGETX3[20] to give radial pair distribution functions. Further details of the reconstruction and corrections are given in ESI section S2.

Rietveld refinements were carried out using a "surface" strategy (i.e. treating all the diffractograms as a single 3D "surface" of data with some parameters linked for the entire dataset but no use of parametric equations) based on the parametric Rietveld method in TOPAS V5[21]. Background, lattice parameters, atom positions, peak broadening (Lorentzian crystallite size based on a fundamental parameters peak shape) thermal parameters and scale factors were refined simultaneously for all diffraction patterns in each group (usually a complete slice of the tomogram[10]) while the zero error and tan-θ broadening[22] were refined as single parameters for the whole dataset. Adsorption was handled using the parallel beam capillary correction in TOPAS with a fixed adsorption value. A typical fit is shown in the ESI (Figure S16) along with the Rwp values for the fits (table S2).

The size values from the Rietveld analysis are not absolute as we could not fully characterise the instrumental resolution for ID15A; the trends however are real. (crystallite size is used to indicate the presence of crystalline Na3P as the Rietveld scale factor is highly influenced by increases in the peak width when there are no longer clear Bragg peaks in the patterns and therefore fails to clearly indicate the appearance and disappearance of the crystalline phase)

The PDF data were analysed using routines adapted from diffpy-CMI[23]. Corrections and model design are described in ESI section S4. Scale factors were refined for all phases and lattice parameters were refined for the Na3P. A global bond length variation parameter was refined for the NaP and P clusters. Thermal parameters for the Na and P were constrained to be constant during all fits and across all of the phases. The instrumental parameter "qdamp" was held constant during all refinements, as was "delta2" for each phase.

Total energies were calculated by the projected-augmented plane-wave (PAW) implementation of the Vienna *ab initio* simulation package (VASP).[24] The methods used for the calculations are described more fully in ESI section S3.

References

[1]   C. P. Grey, J. M. Tarascon, *Nat Mater* **2017**, *16*, 45-56.

[2]   a G. Zhang, T. Xiong, L. He, M. Yan, K. Zhao, X. Xu, L. Mai, *Journal of Materials Science* **2017**, *52*, 3697-3718; b J. Lu, T. Wu, K. Amine, *Nature Energy* **2017**, *2*, 17011; c X. Wei, X. Wang, Q. An, C. Han, L. Mai, *Small Methods* **2017**, *1*, 1700083-n/a.

[3]   T. Egami, S. J. L. Billinge, *Underneath the Bragg Peaks*, Pergamon,**2003**.

[4]   P. K. Allan, J. M. Griffin, A. Darwiche, O. J. Borkiewicz, K. M. Wiaderek, K. W. Chapman, A. J. Morris, P. J. Chupas, L. Monconduit, C. P. Grey,*J. Am. Chem. Soc.* **2016**, *138*, 2352-2365.

[5]   a O. J. Borkiewicz, B. Shyam, K. M. Wiaderek, C. Kurtz, P. J. Chupas, K. W. Chapman, *J. Appl. Cryst.* **2012**, *45*, 1261-1269; b Y.-Y. Hu, Z. L. K-W. Nam, O. J. Borkiewicz, J. Cheng, X. Hua, M. T. Dunstan, X. Yu, K. M. Wiaderek, L.-S. Du, K. W. Chapman, P. J. Chupas, X.-Q. Yang, P. Grey, *Nat Mater* **2013**, *12*, 1130-1136; c K. M. Wiaderek, O. J. Borkiewicz, N. Pereira, J. Ilavsky, G. G. Amatucci, P. J. Chupas, K. W. Chapman, *J. Am. Chem. Soc.* **2014**, *136*, 6211-6214.

[6]   S. D. M. Jacques, M. Di Michiel, S. A. J. Kimber, X. Yang, R. J. Cernik, A. M. Beale, S. J. L. Billinge, *Nat Commun* **2013**, *4*.

[7]   a D. P. Finegan, M. Scheel, J. B. Robinson, B. Tjaden, I. Hunt, T. J. Mason, J. Millichamp, M. Di Michiel, G. J. Offer, G. Hinds, D. J. L. Brett, P. R. Shearing, *Nat Commun* **2015**, *6*; b M. Ebner, F. Marone, M. Stampanoni, V. Wood, *Science* **2013**, *342*, 716-720; c D. P. Finegan, E. Tudisco, M. Scheel, J. B. Robinson, O. O. Taiwo, D. S. Eastwood, P. D. Lee, M. Di Michiel, B. Bay, S. A. Hall, G. Hinds, D. J. L. Brett, P. R. Shearing, *Advanced Science* **2016**, *3*, 1500332-n/a.

[8]   a P. Pietsch, M. Hess, W. Ludwig, J. Eller, V. Wood, *Scientific Reports* **2016**, *6*; b G. Tonin, G. Vaughan, R. Bouchet, F. Alloin, M. Di Michiel, L Boutafa, J.-F. Colin, C. Barchasz, *Scientific Reports* **2017**, *7*, 2755.

[9]   K. M. O. Jensen, X. H. Yang, J. V. Laveda, W. G. Zeier, K. A. See, M. Di Michiel, B. C. Melot, S. A. Corr, S. J. L. Billinge, *J. Electrochem. Soc.* **2015**, *162*, A1310-A1314.

[10]   D. S. Wragg, M. G. O'Brien, M. Di Michiel, F. Lonstad-Bleken, *J. Appl. Cryst.* **2015**, *48*, 1719-1728.

[11]   a J. Qian, X. Wu, Y. Cao, X. Ai, H. Yang, *Angew. Chem. Int. Ed. Engl.* **2013**, *52*, 4633-4636; b Y. Kim, Y. Park, A. Choi, N.-S. Choi, J. Kim, J. Lee, J. H. Ryu, S. M. Oh, K. T. Lee, *Advanced Materials* **2013**, *25*, 3045-3049.

[12]   a T. Ramireddy, T. Xing, M. M. Rahman, Y. Chen, Q. Dutercq, D. Gunzelmann, A. M. Glushenkov, *Journal of Materials Chemistry A* **2015**, *3*, 5572-5584; b G.-L. Xu, Z. Chen, G.-M. Zhong, Y. Liu, Y. Yang, T. Ma Y. Ren, X. Zuo, X.-H. Wu, X. Zhang, K. Amine, *Nano Letters* **2016**, *16*, 3955-3965.

[13]   M. Mayo, K. J. Griffith, C. J. Pickard, A. J. Morris, *Chem. Mater.* **2016**, *28*, 2011-2021.

[14]   J. Sun, H.-W. Lee, M. Pasta, H. Yuan, G. Zheng, Y. Sun, Y. Li, Y.   Cui, *Nat Nano* **2015**, *10*, 980-985.

[15]   R. Shannon, *Acta Crystallographica Section A* **1976**, *32*, 751-767.

[16]   J. Sottmann, M. Herrmann, P. Vajeeston, Y. Hu, A. Ruud, C.   Drathen, H. Emerich, H. Fjellvåg, D. S. Wragg, *Chem. Mater.* **2016**, *28*, 2750- 2756.

[17]   K. A. Hays, N. A. Banek, M. J. Wagner, *Meeting Abstracts* **2015**, *MA2015-01*, 650.

[18]   H. Kim, H. Kim, H. Kim, J. Kim, G. Yoon, K. Lim, W.-S. Yoon, K.   Kang, *Advanced Functional Materials* **2016**, *26*, 5042-5050.

[19]   a S. D. M. Jacques, M. M. Di, A. M. Beale, T. Sochi, M. G. O'Brien, L. Espinosa-Alonso, B. M. Weckhuysen, P. Barnes, *Angew. Chem., Int. Ed.* **2011**, *50*, 10148-10152, S10148/10141-S10148/10111;   b   M. G. O'Brien, S. D. M. Jacques, M. D. Michiel, P. Barnes, B. M. Weckhuysen, A. M. Beale, *Chem. Sci.* **2012**, *3*, 509-523.

[20]   P. Juhas, T. Davis, C. L. Farrow, S. J. L. Billinge, *J. Appl. Cryst.* **2013**, *46*, 560-566.

[21]   a A. A. Coelho, Bruker AXS, **2014**; b G. W. Stinton, J. S. O. Evans, *J. Appl. Cryst.* **2007**, *40*, 87-95.

[22]   M. G. O'Brien, A. M. Beale, S. D. M. Jacques, M. Di Michiel, B. M. Weckhuysen, *Applied Catal. A.* **2011**, *391*, 468-476.

[23]   C. L. Farrow, P. Juhas, J. W. Liu, D. Bryndin, E. S. Božin, J. Bloch, P.   Th, S. J. L. Billinge, *Journal of Physics: Condensed Matter* **2007**, *19*, 335219.

[24]   a G. Kresse, J. Furthmüller, *Physical Review B* **1996**, *54*, 11169-11186; b G. Kresse, J. Furthmüller, *Computational Materials Science* **1996**, *6*, 15-50.
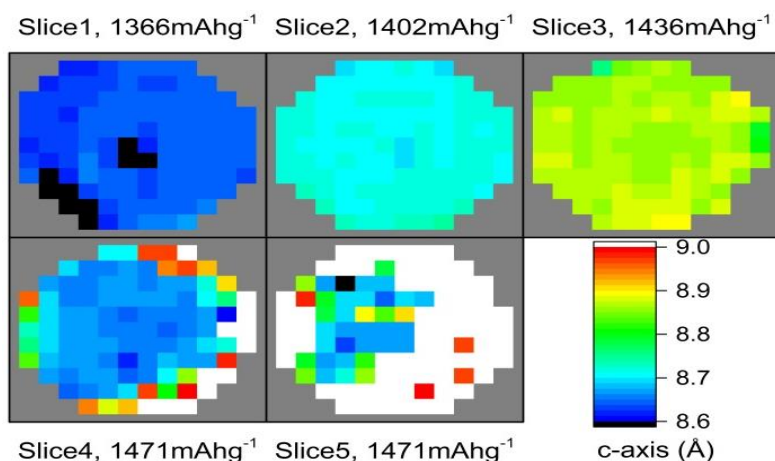
Figures

Figure 1. Tomographic slices at the end of the second sodiation, reconstructed on the *c*-axis of Na$_3$P extracted by parametric Rietveld methods. Slices (thickness 16 μm) were collected a different distances from the current collector. Slice 1 is closest to the current collector and slices 4 and 5 partly cut into the glass fibre separator. Note that *c*-axis variation within the slices is minimal. The *c*-axis variations between the slices are probably due in the most part to changes in the charge state during the 7 min acquisition time per slice. Electrochemical cycling curves showing the points at which each tomographic slice was acquired are shown in the ESI (Figure S19).
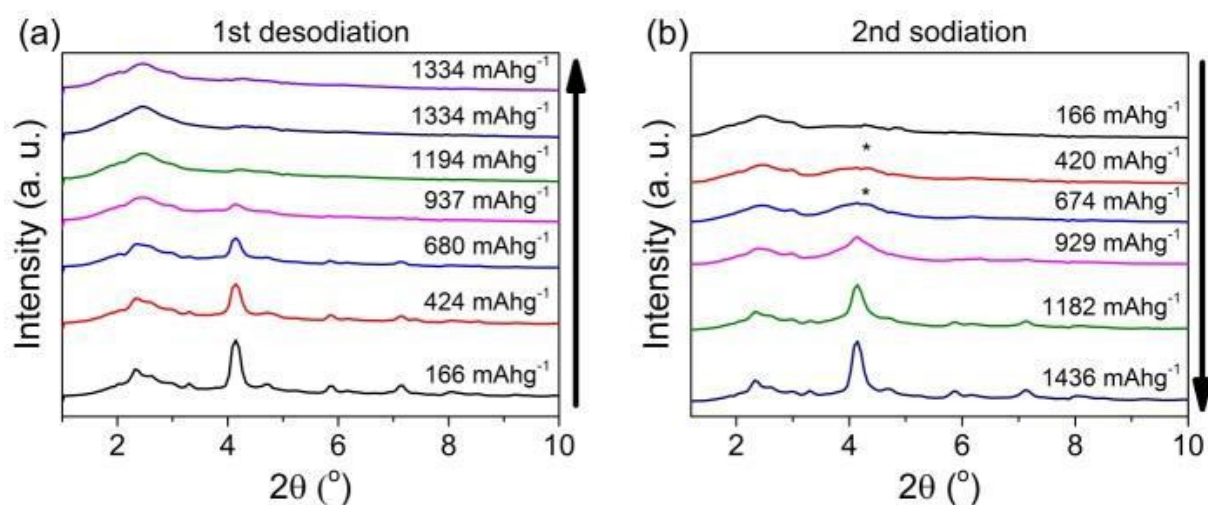
Figure 2. Reconstructed XRD data of the voxel at position (15, 15) in tomographic slice 3 at different charge states for the first desodiation (a) and second sodiation (b). The broad feature observed at 2θ ≈ 4 ° is marked with *.
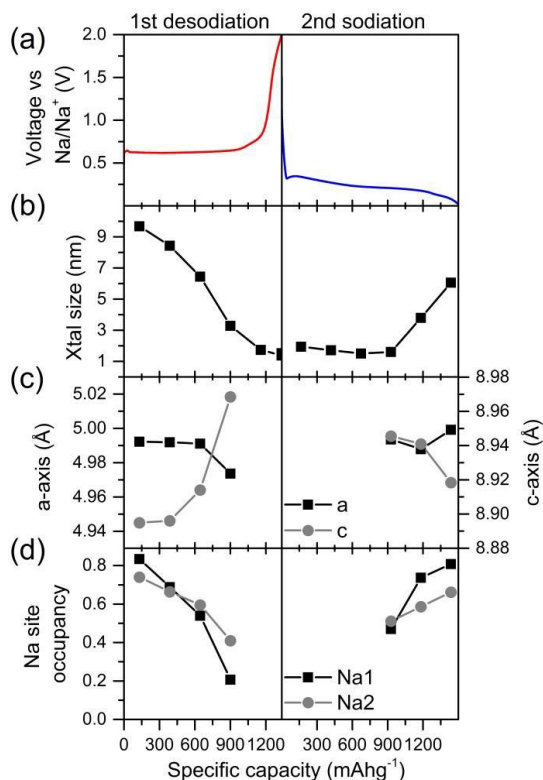
Figure 3. Voltage profiles for desodiation and sodiation (a) and data from Rietveld refinements of Na3P in voxel at position (15,15) of tomographic slice 3: crystallite size (b), lattice parameters (c) and Na site occupancy (d). Lattice parameter and site occupancy results from diffractograms collected at charge states where crystalline Na3P is not present are omitted.
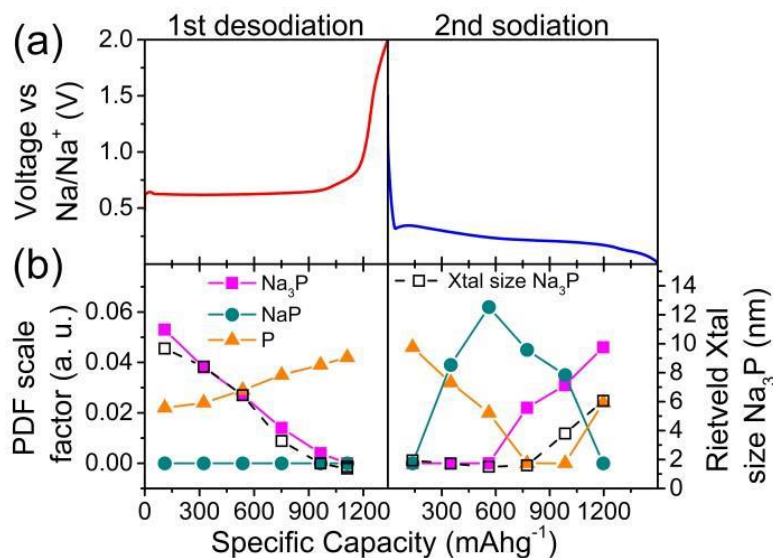

Figure 4. Voltage profiles for desodiation and sodiation (a) and plots of the PDF scale factor for all phases (b). Crystallite size obtained from Rietveld refinement of Na3P is plotted for comparison.
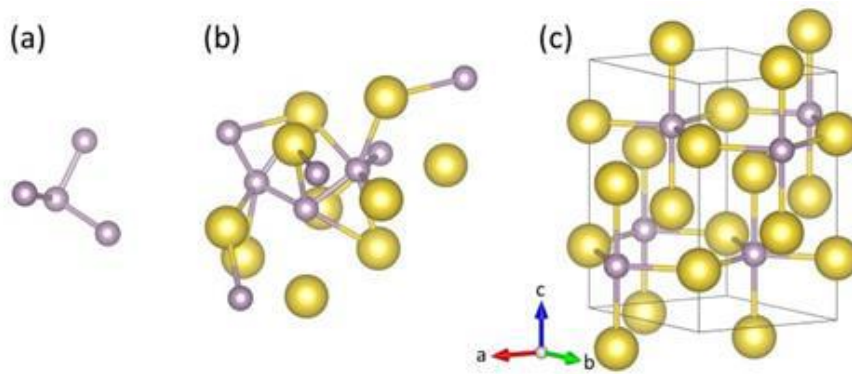
Figure 5. Models used in the PDF analysis: (a) amorphous P nano-cluster, (b) amorphous NaP nano-cluster and (c) crystalline Na3P.
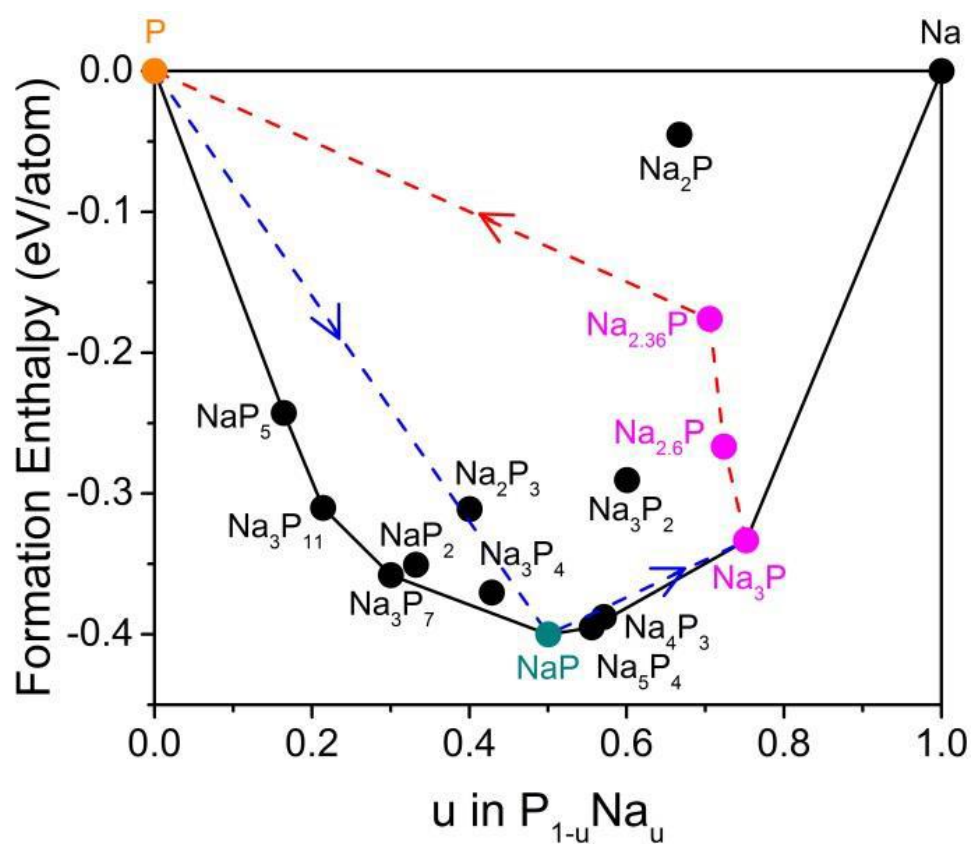

Figure 6. DFT energy hull diagram showing the lowest energy phases in the P-Na phase diagram and formation enthalpies for Na deficient Na3-xP structures (coloured in magenta). The black line indicates the lowest energy route, while the blue and red dotted lines show the observed routes of desodiation and sodiation, respectively.